

# Investigation of Rock Mass Stability Around the Tunnels in an Underground Mine in USA Using Three-Dimensional Numerical Modeling

Yan Xing<sup>1,2</sup> · P. H. S. W. Kulatilake<sup>3</sup> · L. A. Sandbak<sup>4</sup>

Received: 10 February 2017 / Accepted: 27 September 2017 / Published online: 11 October 2017  
© Springer-Verlag GmbH Austria 2017

**Abstract** The stability of the rock mass around the tunnels in an underground mine was investigated using the distinct element method. A three-dimensional model was developed based on the available geological, geotechnical, and mine construction information. It incorporates a complex lithological system, persistent and non-persistent faults, and a complex tunnel system including backfilled tunnels. The strain-softening constitutive model was applied for the rock masses. The rock mass properties were estimated using the Hoek–Brown equations based on the intact rock properties and the RMR values. The fault material behavior was modeled using the continuously yielding joint model. Sequential construction and rock supporting procedures were simulated based on the way they progressed in the mine. Stress analyses were performed to study the effect of the horizontal in situ stresses and the variability of rock mass properties on tunnel stability, and to evaluate the effectiveness of rock supports. The rock mass behavior was assessed using the stresses, failure zones, deformations around the tunnels, and the fault shear displacement vectors. The safety of rock supports was quantified using the bond shear and bolt tensile failures. Results show that the major fault and weak

interlayer have distinct influences on the displacements and stresses around the tunnels. Comparison between the numerical modeling results and the field measurements indicated the cases with the average rock mass properties, and the  $K_0$  values between 0.5 and 1.25 provide satisfactory agreement with the field measurements.

**Keywords** Tunnel stability · Rock mass properties · Distinct element method · 3D numerical modeling · In situ stress · Rock supports

## 1 Introduction

For an underground mine, the development drifts are used to extract and transport the ore from the mining area. The safety of these tunnels plays important roles on the economy and sustainability of the mine. Understanding the rock mass behavior around the tunnels is critical to select the supports, arrange the suitable construction sequences, and finally help to avoid unnecessary disasters. Minor discontinuities, such as fissures, fractures, joints, and large-scale discontinuities, such as faults, shear zones, dikes, can significantly weaken the strength or increase the deformability of rock masses. The orientation of the discontinuities is critical to the failure modes of underground structures (Hao and Azzam 2005; Jia and Tang 2008; Huang et al. 2013). The high in situ stress is another unfavorable factor that may be encountered in underground problems. It may cause large deformations and failure around the tunnels (Kulatilake et al. 2013; Lin et al. 2015). Additionally, the configuration of the tunnel system, i.e., the distance between adjacent tunnels, heading directions of the tunnels, tunnel dimensions, also has great influences on the stability of surrounding rock masses (Li et al. 2013; Wang et al. 2012; Bhasin et al. 2006). To deal

✉ P. H. S. W. Kulatilake  
kulatila@u.arizona.edu

<sup>1</sup> Department of Mining and Geological Engineering, University of Arizona, Tucson, AZ 85721, USA  
<sup>2</sup> State Key Laboratory for Geomechanics and Deep Underground Engineering, China University of Mining and Technology, Xuzhou 221116, China  
<sup>3</sup> Rock Mass Modeling and Computational Rock Mechanics Laboratories, University of Arizona, Tucson, AZ 85721, USA  
<sup>4</sup> Barrick Gold Inc, Golconda, NV 89414, USA

with problems having the above-mentioned diverse factors, the numerical simulation has been proved as a suitable tool (Jing 2003; Zhu and Zhao 2004).

In continuum modeling, the discontinuities can be modeled as elements with different material properties from the intact rock or as special joint elements (Goodman et al. 1968; Zienkiewicz et al. 1970; Ghaboussi et al. 1973; Gens et al. 1989). Nevertheless, the continuous assumption determines that the material will never be open or broken into pieces (Jing 2003); the joint displacements are restricted to small values. The equivalent continuum method implicitly incorporates the effect of discontinuities. In these models, the rock mass properties can be obtained by scaling the intact rock properties down using some empirical relations (e.g., Hoek and Brown 1997; Barla and Barla 2000).

On the other hand, the application of discrete element method in jointed rock masses has gained progressive attention in recent years. Due to the explicit representation of the discontinuities, the discontinuum modeling is capable to account for the large deformations and rotations, including complete detachment, of discrete blocks. This method, hence, is appropriate for the problems where the discontinuities have significant contributions to the instability of the structures. For example, Hao and Azzam (2005) summarized the faults-associated failures, such as collapse of a large rock mass volume within a fault zone, a slide along a fault plane, falling of blocks formed by faults and other minor discontinuities, as well as long-term rock mass degradation, failure and asymmetric deformations. They claimed that the discrete element method describes the fault behavior in a more realistic way. In addition, the dependence of joint deformation properties on the normal stress has been conformed either in the laboratory tests (Goodman 1974; Barton and Choubey 1977; Bandis et al. 1983; Malama and Kulatilake 2003; Kulatilake et al. 2016) or in the field (Cui et al. 2016). An appropriate joint constitutive model which can reveal the intrinsic joint behavior is of importance to predict the displacements and stresses in complex practical problems (Souley et al. 1997). The distinct element method (DEM), proposed by Cundall (1971, 1988) and Hart et al. (1988), is such a competent method to take care of the complex constitutive behaviors for both the rock masses and the joints.

Previous studies on the stability of tunnels or other underground structures using DEM have been addressed through UDEC (Cundall 1980) and 3DEC (Cundall 1988; Hart et al. 1988), for two- and three-dimensional modeling, respectively. For instance, the UDEC was used as the tool by Chryssanthakis et al. (1997) to investigate the influences of the fiber-reinforced shotcrete and the construction sequences on the stability of the tunnels, by Bhasin and Høeg (1997) to study the rock mass behavior of a large cavern, by Shen and Barton (1997) to study the effects of joint spacing and joint orientation on the disturbed zones (failure zone, open zone,

and shear zone) around tunnels and by Gao et al. (2014) to simulate the roof shear failure in coal mine roadways tracking the newly formed contacts during excavation. Wang et al. (2012) performed three-dimensional analyses using discontinuum and continuum models in 3DEC. Using the joint data collected by laser scanning (Lidar), Fekete and Diederichs (2013) developed a discontinuum model using 3DEC to simulate the structurally controlled failure around a tunnel in a blocky rock mass. In the research of Shreedharan and Kulatilake (2016), 3DEC was used to investigate the stability of the tunnels with two different shapes in a deep coal mine in China; the effectiveness of support system was evaluated by implementing the instantaneous and the more realistic stress-relaxation installation routines. Cui et al. (2016) carried out seismic analysis for an underground chamber by using 3DEC. In their numerical model, a large geological discontinuity was modeled by the continuously yielding joint model; they found that the discontinuity had major influence on the deformations around the chamber.

Under the circumstances where the factors, such as structures, lithologies, in situ stress field, are not proper to be simplified on one plane, the three-dimensional modeling is necessary. In addition, the importance of the actual stress path in the rock masses due to the excavation and its influence on the yielding zones around the tunnels have been stressed by Cai (2008). Cantieni and Anagnostou (2009) pointed out the ground pressures and deformations are normally underestimated in the plane strain analysis. To capture the realistic rock mass response to excavation, the three-dimensional modeling is necessary to incorporate the sequence of supporting and excavation.

In this study, three-dimensional stress analyses were performed to understand the deformation and failure mechanisms of the rock masses and to evaluate the overall stability around the tunnels for an underground mine in the USA. To explicitly represent the major discontinuities (faults) that exist in the field, the distinct element method (DEM) was utilized. A three-dimensional numerical model was generated based on the real geological, geotechnical, and mine construction information. The features of the inclined lithologies, the faults, the weak interlayer as well as the complex tunnel system are included. The rock mass properties which are the combined properties of the intact rock and minor discontinuities were estimated by using the Hoek–Brown equations (Hoek and Brown 1997). The fault parameters were estimated from laboratory testing on the smooth joints. The strain-softening constitutive model and the continuously yielding joint model were applied for the blocks and the discontinuities, respectively. Sequential excavation, rock supports, and backfilling were implemented. The effect of the in situ lateral stress ratio ( $K_0$ ) and the rock mass properties on the stability and deformation around the tunnels was investigated. The performance of the rock supports was

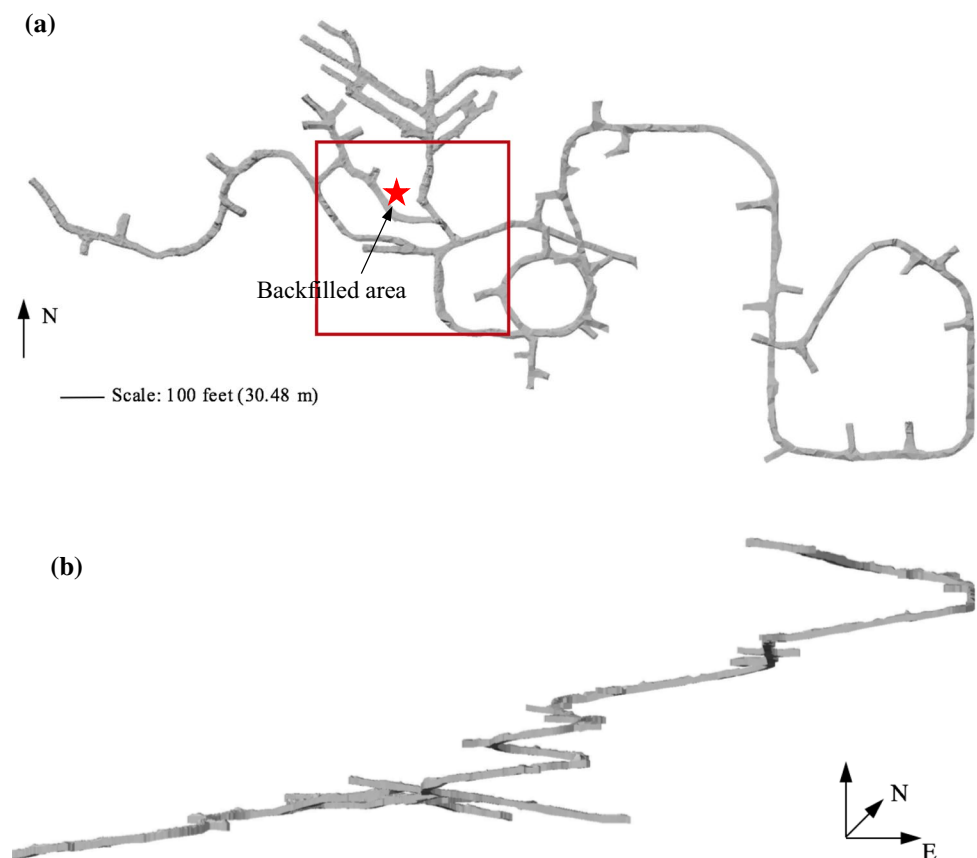
assessed through the reductions in deformations and failure zones around the tunnels and through the safety of supports. Finally, the numerical modeling results were compared with the field monitoring data.

## 2 Description of the Mine Site and the Tunnel System

The studied mine site is an operating underground mine in the USA. The average elevation of ground surface is around 5500 feet (1676.4 m). The deposits are sediment hosted and are generally controlled by the intersection of mineralized faults and stratigraphic units. The ore bodies are dipping approximately  $25^{\circ}$ – $45^{\circ}$  with a low rock mass quality in the ore zones. Stratigraphy mainly consists of carbonaceous mudstones and limestones, tuffaceous mudstones and limestones, polyolithic megaclastic debris flows, fine-grained debris flows and basalts, all parts of Cambrian-Ordovician Comus formation. Near surface units include pillow basalt, auto-brecciated and hyaloclastite basalt (greenstone), argillites and chert of the Valmy formation. All the units are intruded by the fine-grained to porphyritic granodiorite dikes and sills.

The development drifts used to extract and transport the ores were driven around or through major fault zones. Figure 1 shows, respectively, the plan and elevation views of one of the tunnel systems. The interested area is located at the elevation of 2975–3375 feet (906.7–1028.7 m), inside the red square of Fig. 1a. It extends 400 feet (122 m) along the east–west and south–north directions. Within this area, the major lithology Oc5 is formed of limestone with thinly laminated to thinly bedded mudstones. The intruded dacite dike (the second lithology) has the angles of  $25^{\circ}$ – $45^{\circ}$  dipping eastwards. Major structures include the high angle faults striking NW–SE and dipping southwest, the sets that strike NE–SW and dip northwest, and the low-angle faults dipping to the east with  $20^{\circ}$ – $40^{\circ}$ . Backfilling activities were located at the upper-left region and above the open tunnels (Fig. 1a). The rock mass ratings (RMR) range from 25 to 55 according to Bieniawski (1976). Low RMR values have been assigned for the dacite rock masses. The rock masses within the area are in dry condition. The applied bolt supports include resin bolts, swellex/super swellex, split sets, and cable bolts. No in situ stress measurement has been conducted at this mine. Tape extensometers and multiple point extensometers were installed to record the convergence and in-rock displacements of the tunnels.

**Fig. 1** The overall tunnel system at the underground mine: **a** plan view; **b** elevation view (seeing from the south)



### 3 Estimation of the Rock Mass Properties

In this paper, the properties of intact rock and minor discontinuities are combined together and represented as rock mass properties. The rock masses in Oc5 (lithology 1) have a wide range of RMR values, from 25 to 55 (poor to fair), while the rock masses belonging to the dike (lithology 2) is in a relatively poor condition with RMR values in the range of 25–40. The average RMR values for the two lithologies are, respectively, 40 and 32.5. The rock mass properties of the two lithologies were estimated using the empirical formulas proposed by Hoek et al. (2002), and Hoek and Diederichs (2006). According to Hoek and Brown (1997), the GSI (Geological Strength Index) (Hoek 1994) can be estimated from the 1976 version of RMR values with the ground water rating set to 10 (dry) and the adjustment for joint orientation set to 10 (very favorable). Laboratory testing results were available for the intact rock.

The deformation modulus of the rock mass was determined by the following equation:

$$E_{rm} = E_i \left( 0.02 + \frac{1 - D/2}{1 + e^{((60+15D-GSI)/11)}} \right) \tag{1}$$

where  $E_i$  is the Young’s modulus of the intact rock;  $D$  is a factor describing the disturbance degree of the rock mass subjected by blast damage and stress relaxation. It varies from 0 for undisturbed rock masses to 1 for very disturbed rock masses. In this research,  $D$  was set to 0.1, representing the situation of low disturbance from blasting.

The equations to estimate the equivalent Mohr–Coulomb parameters, friction angle ( $\phi$ ) and cohesion ( $c$ ), are given by

$$\phi = \sin^{-1} \left[ \frac{6am_b(s + m_b\sigma_{3n})^{a-1}}{2(1+a)(2+a) + 6am_b(s + m_b\sigma_{3n})^{a-1}} \right] \tag{2}$$

$$c = \frac{\sigma_{ci}[(1+2a)s + (1-a)m_b\sigma_{3n}](s + m_b\sigma_{3n})^{a-1}}{(1+a)(1+2a)\sqrt{1 + (6am_b(s + m_b\sigma_{3n})^{a-1})/(1+a)(1+2a)}} \tag{3}$$

where the rock mass constants  $m_b$ ,  $s$ , and  $a$  can be calculated from Eqs. (4)–(6);  $\sigma_{3n}'$  is a factor related to the maximum confining stress,  $\sigma_{3max}'$ , within which the fitting relation between the Hoek–Brown and the Mohr–Coulomb criterion is considered. Hoek et al. (2002) provided guidelines to estimate the value of  $\sigma_{3n}'$  for deep tunnels. According to

that, the range of the confining stress used to obtain  $c$  and  $\phi$  in this paper is 0–8 MPa.

$$m_b = m_i \exp\left(\frac{GSI - 100}{28 - 14D}\right) \tag{4}$$

$$s = \exp\left(\frac{GSI - 100}{9 - 3D}\right) \tag{5}$$

$$a = \frac{1}{2} + \frac{1}{6}(e^{-GSI/15} - e^{-20/3}) \tag{6}$$

The  $m_i$  in Eq. (4) is the intact rock parameter, which can be obtained from the triaxial tests.

There are no available empirical equations suggested for the estimation of rock mass Poisson’s ratio. However, Kulatilake et al. (2004) found that the Poisson’s ratio increased about 21% from intact rock for rock masses due to the existence of discontinuities. The Poisson’s ratio ( $\mu_r$ ) of the rock mass in this study is assumed to be 1.2–1.4 times of that of the intact rock. Several references were reviewed to estimate reasonable rock mass tensile strength values. According to Wu and Kulatilake (2012), the achieved rock mass tensile strength is about 35% of the intact rock for a study conducted on estimating representative elementary volumes and equivalent continuum strength and deformability parameter values for a limestone rock mass. By calibrating the strength and deformability parameters based on the field monitoring data, Shreedharan and Kulatilake (2016) concluded in their research that the estimated rock mass strength is between 38 and 44% of the intact rock. In the study of Huang et al. (2017), the estimated tensile strength of the rock masses based on the Hoek and Brown criterion was between 24 and 35% of the intact rock. Based on the aforementioned results, in this study, the rock mass tensile strength is scaled down to 30% of the intact value.

The calculated Hoek–Brown constants and the estimated rock mass property values are given in Tables 1 and 2, respectively.

## 4 Three-Dimensional Numerical Modeling

### 4.1 Development of the Numerical Model

In this paper, 3DEC Version 4.1 software package (Itasca Consulting Group and Inc 2007) was used to build the numerical model and to perform the stress analysis. The three-dimensional model is a cube with the dimensions of 122 m in three directions. The origin of the coordinates is

**Table 1** Estimated Hoek–Brown constants for the rock masses

Lithology	GSI	$m_i$	$D$	$m_b$	$s$	$a$
Oc5	40	8.94	0.1	0.937	1.0e-3	0.511
Dike	32.5	5.03	0.1	0.398	4.3e-4	0.519

located at the center of the model;  $z$  axis is vertical with the positive direction upward; positive  $y$  and  $x$  axes are in accord with the north and east directions in the field (Fig. 2a). The numerical model consists of two lithologies, as shown in Fig. 2a, where lithology 1 (Oc5) is shown in blue, and lithology 2 (the dike) is the thin layer shown in light green. Figure 2b shows the detailed weak layer, which is built as inclined and non-planar. Figure 3 shows the faults and the tunnel system built inside the numerical model, which is represented by the outline box. The major

non-persistent fault, striking  $N53^\circ W$  and dipping  $60^\circ$  to southwest, terminates inside the model and intersects with the tunnel system. Several persistent faults cut the model in the left upper part and in the bottom area (Fig. 3a). The tunnel system, including both open and backfilled ones, extends to the side boundaries and ranges from  $-10$  to  $12$  m in the  $z$  direction. Figure 3b presents the view seeing from the upper northeast; most of the backfilling activities took place on the footwall of the major fault. Two kinds of tunnel cross sections are applied in the numerical model,

**Table 2** Physical and mechanical property values to represent the rock masses in the numerical model

Lithology	Density ( $\text{kg/m}^3$ )	Bulk modulus (GPa)	Shear modulus (GPa)	Friction angle ( $^\circ$ )	Cohesion (MPa)	Tensile strength (MPa)
Oc5	2743	8.11	3.74	35.5	1.96	2.56
Dike	2380	1.11	0.57	25.6	1.20	1.15
Backfilling	2146	0.73	0.55	44.0	0.69	0.61

**Fig. 2** Lithologies built in the numerical model: **a** lithologies; **b** dike layer

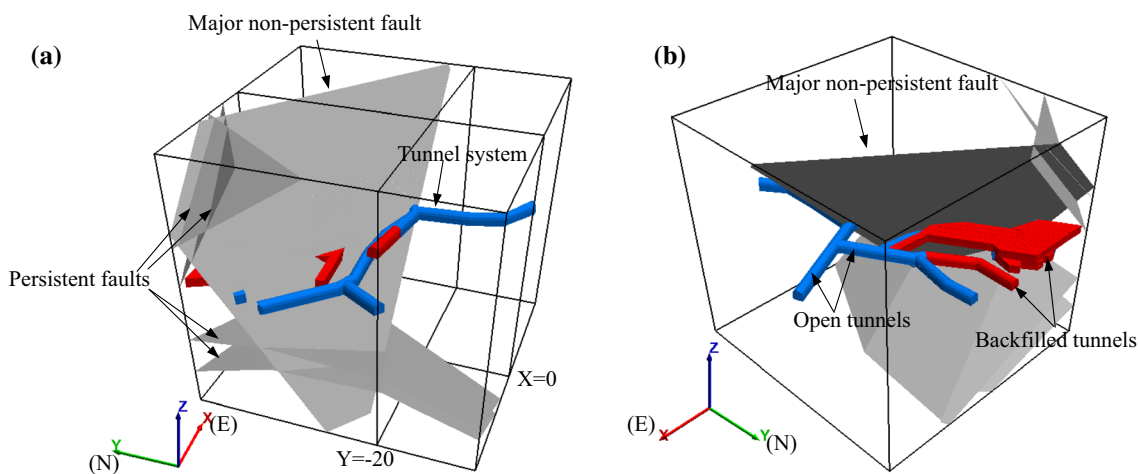
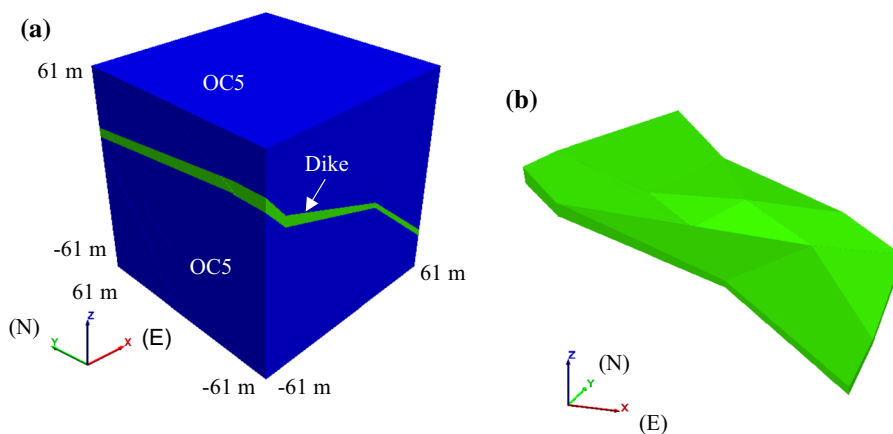


**Fig. 3** Faults and tunnel system built in the numerical model (represented by the outline box) seeing from views of **a** upper southwest and **b** upper northeast

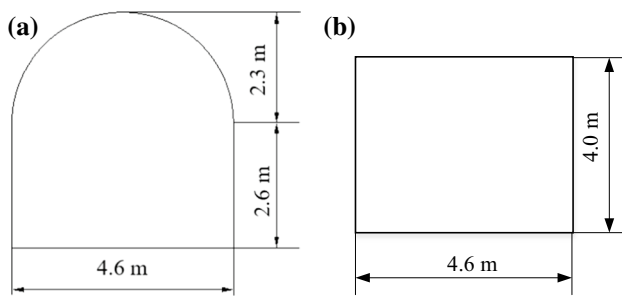


**Fig. 4** Dimensions of the **a** horseshoe tunnel and **b** rectangular tunnel

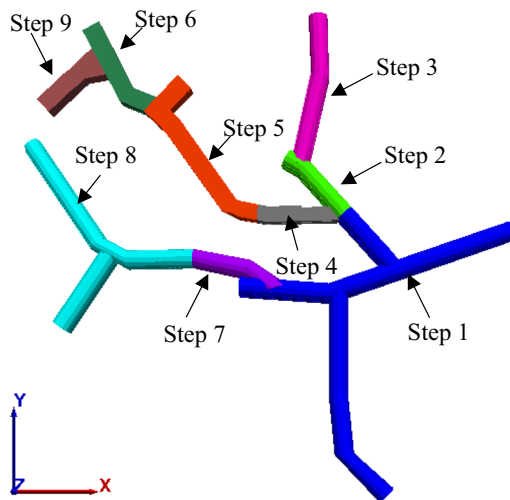


**Fig. 5** Plan view of the excavation sequence of the open tunnels in the numerical model

as shown in Fig. 4. Most of the backfilled tunnels in the northern part were excavated in the rectangular shape (Fig. 3b).

In the presence of non-persistent faults, the domain of the numerical model does not get discretized into polyhedral. On the other hand, to perform stress analysis with 3DEC version 4.1, it is necessary to discretize the domain into polyhedral. This is achieved by inserting artificial joints that behave as the rock material. Such joints are known as fictitious joints (Kulatilake et al. 1992). After an extensive investigation, Kulatilake et al. (1992) provided guidelines to assign parameter values for these fictitious joints.

According to the excavations conducted in the field, the open tunnels were excavated from the year of 2004–2010, which was divided into nine steps in the numerical model, as shown in Fig. 5. The construction of the backfilled areas was also numerically simulated step by step according to the field sequence. Three rounds of the rock supports were installed for the tunnels. Figure 6a, b shows the two arrangements of the first installation. Arrangement 1 includes three 2.44 m

resin bolts on the roof and eight 1.83 m split sets on the ribs, while arrangement 2 includes four resin bolts on the roof and eight split sets on the ribs. The in-plane spacing and the layout of the bolts are shown in Fig. 6a, b. The two arrangements were installed alternately along the tunnel axis at a spacing of 1.2 m. Figure 6c, d shows the two arrangements of the second installation (cable bolts), where the difference is the number of bolts applied on the roof. Both the in-plane spacing and out-of-plane spacing are 1.8 m. The third installation (swellex bolts) is presented in Fig. 6e. The length of the bolts on the ribs is 3.7 and 6.1 m on the roof. Both the in-plane spacing and out-of-plane spacing are 1.8 m. The rock bolts were simulated using the “Cable” structure element in 3DEC (Itasca Consulting Group and Inc 2007). Table 3 gives the material property values used for the rock supports in the numerical model. They were estimated based on the information provided by the mining company, the manufactures, and the suggestions given in the manual of 3DEC (Itasca Consulting Group and Inc 2007). The geometry and spacing of the bolt supports for the rectangular tunnels are similar to that applied for the horseshoe tunnels. Due to the high cost of computation time, instantaneous installation of the rock supports was adopted after each excavation.

Due to the existence of the inclined weak layer and the faults, the in situ stresses were obtained by applying boundary stresses and performing numerical modeling (Tan et al. 2014a, b; Xing et al. 2017). The depth of the top boundary of the numerical model is about 647.7 m; based on the average overburden density of 2700 kg/m<sup>3</sup>, a vertical stress of 17.5 MPa was applied at the top to simulate the gravitational loading of the overburden strata, as shown in Fig. 7. The roller boundary condition (no velocity or displacement) was specified at the bottom boundary. For lateral boundaries, the roller boundary condition was applied on one side and the stress boundary condition was applied on the other side for both *x* and *y* directions (Fig. 7). Gravity gradient was applied to the whole model. The horizontal stress ( $\sigma_h$ ) was calculated based on the lateral stress ratio ( $K_h = K_H = K_0$ ) of 0.5, 0.75, 1.0, 1.25, 1.5, and 2.0.

The backfilling material is made of waste rock with 5.8% cement, 1.95% fly ash, 7.8% binder, and 0.42 ratio of water/binder. The material property values used for the backfilling material in the numerical model are given in Table 2 according to the laboratory testing results of the backfill cylinders.

The average quality rock masses ( $25 < \text{GSI} < 75$ ) usually show a strain-softening behavior in the post-failure region (Hoek and Brown 1997). Such behavior can play a significant role governing the rock mass response around the excavations (Hoek and Brown 1997; Egger 2000). In this study, the strain-softening constitutive model based on the Mohr–Coulomb criterion was applied for the rock masses. As shown in Fig. 8, the degradation of strength parameters (cohesion, friction angle, and tensile strength) after yielding

**Fig. 6** Bolt supports that applied in the numerical model: **a** the first installation—arrangement 1 (3 resin bolts on the roof; 8 split sets on the ribs) **b** the first installation—arrangement 2 (4 resin bolts on the roof; 8 split sets on the ribs); **c** the second installation—arrangement 1 (3 cable bolts on the roof); **d** the second installation—arrangement 2 (2 cable bolts on the roof); **e** the third installation (5 Swellex bolts on the roof; 2 Swellex bolts on the ribs)

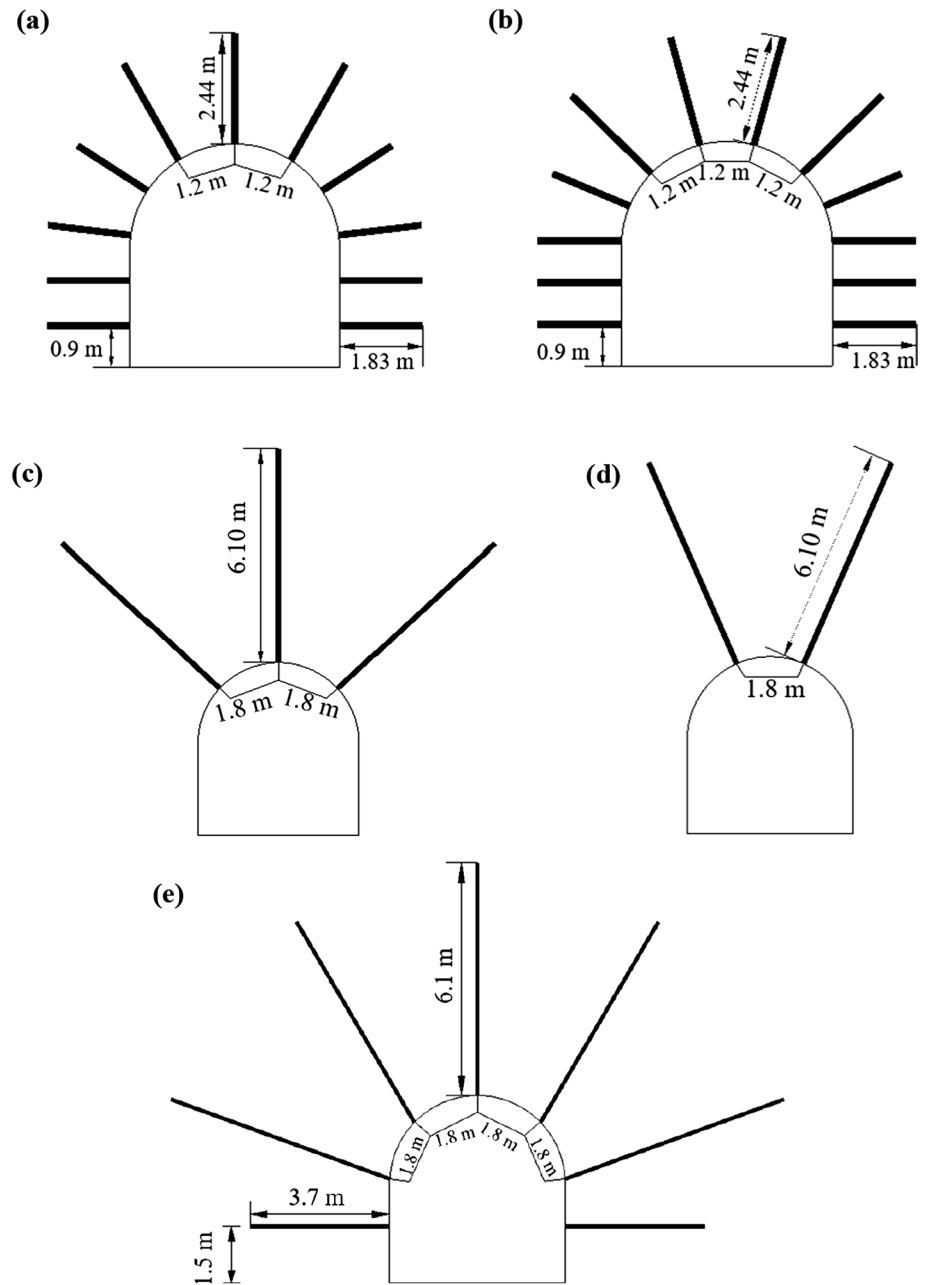


**Table 3** Material property values used for rock supports in the numerical model

Type of support (see Fig. 5a–e)	Young's modulus of bolt (GPa)	Bolt diameter (mm)	Cross-sectional area of bolt (m <sup>2</sup> )	Tensile yield capacity of the bolt (KN)	Bond shear stiffness (MN/m/m)	Bond strength (KN/m)
Split sets	200	39	1.19e−3	140	100	50
Resin bolts	200	22	3.8e−4	230	1350	200
Cable bolts	100	12.7	1.27e−4	188	5440	800
Swellex bolts	200	45	1.59e−3	220	200	300

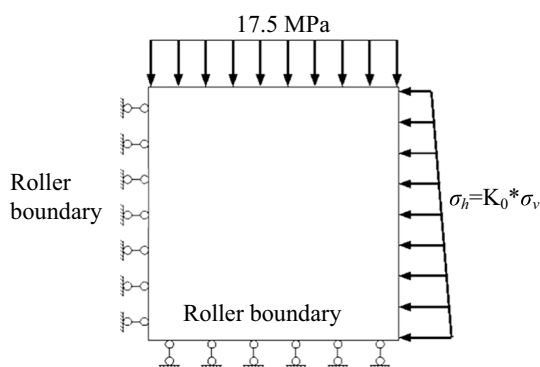


Fig. 7 Boundary conditions applied on the numerical model

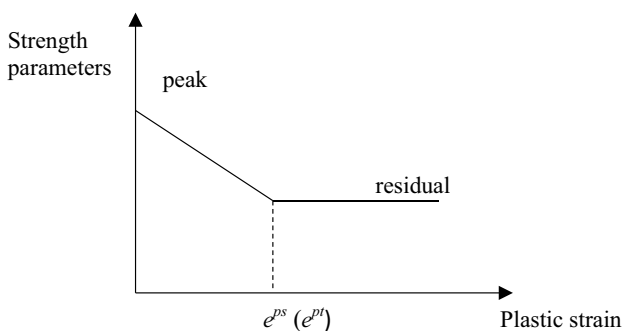


Fig. 8 Post-failure behavior of the strain-softening model

Table 4 Strain-softening property values of the rock masses in the numerical model

Post-failure parameter	Oc5	Dike
Residual friction angle, $\phi_r$ (°)	26.4	21.8
Residual cohesion, $C_r$ (MPa)	0.66	0.60
Residual tensile strength, $\sigma_{tr}$ (MPa)	0.86	0.58
$e^{ps}$ ( $e^{pl}$ ) (milli strain)	3	5

$e^{ps}$ ,  $e^{pl}$  are the plastic strain parameters defined in the manual of 3DEC

is represented in terms of the plastic strain parameters,  $e^{ps}$  and  $e^{pl}$  (Itasca Consulting Group and Inc 2007). Due to the lack of laboratory test data about the post-failure behavior of the rock masses in this research, some references (Hajj-abdolmajid et al. 2002; Ray 2009; Alejano et al. 2012) were reviewed to estimate the strain-softening property values, as given in Table 4.

The uniaxial compression tests on a standard cylindrical sample with a horizontal joint (Kulatilake et al. 2016) and the direct shear tests were carried out for smooth joints in the Geomechanics Laboratory at the University of Arizona. Laboratory results showed that the relation between the normal stress and joint normal displacement is an exponential function. This leads to a linear relation between the joint normal stiffness (JKN) and normal stress. A similar relation exists between the joint shear stiffness (JKS) and the normal stress. The reader is referred to Kulatilake et al. (2016) to obtain the details pertaining to the laboratory test results and these relations. Hence the property values given for JKN and JKS of faults in Table 4 are the coefficients from equations  $JKN = \text{coefficient} * \text{normal stress}$ . Due to the influences of filling material and aperture, the faults in the field could be significantly weaker than the smooth joints in the laboratory. Thus, the property values used for the faults (Table 5) were taken as the half of the property values obtained for the smooth joints.

As previously mentioned, the presence of the non-persistent fault and the non-planar lithology interfaces requires addition of fictitious joints (Kulatilake et al. 1992) to discretize the numerical model domain into polyhedral prior to performing stress analyses using 3DEC version 4.1 code. As far as the mechanical behavior is concerned, these fictitious joints should behave as the respective rock masses of the two lithologies. The mechanical property values of fictitious joints were estimated using the method suggested by Kulatilake et al. (1992), where 0.008 was assigned to  $G_f/JKS$ , and 2.5 to the ratio  $JKN/JKS$ ; the same strength parameter values were used for the rock masses and the fictitious joints. The mechanical property values of interfaces were estimated by first calculating the average values between the two materials and then using the

Table 5 Mechanical property values used for discontinuities in the numerical model

Joint type	Normal stiffness (GPa/m)	Shear stiffness (GPa/m)	Friction angle (°)	Cohesion (MPa)	Tensile strength (MPa)
Fault in Oc5	$6.48 * \sigma_n^a$	$0.81 * \sigma_n^a$	14	0	0
Fault in dike	$10.34 * \sigma_n^a$	$1.01 * \sigma_n^a$	14	0	0
Discontinuity interfaces between Oc5 and Dike	673.8	269.5	30.6	1.58	1.86
Fictitious joints in Oc5	1169.5	467.8	35.5	1.96	2.56
Fictitious joints in Dike	178.2	71.3	25.6	1.20	1.15

<sup>a</sup> $\sigma_n$  is the normal stress in MPa



forementioned method suggested by Kulatilake et al. (1992). The discontinuity interfaces were considered as well-bonded interfaces with gradual transition of material properties rather than weakness planes (Xing et al. 2017). Table 5 gives the mechanical property values of all the discontinuities.

The continuously yielding joint model was applied to simulate the joint behavior of the faults in the numerical model. This joint model can model the nonlinear behavior, such as joint shearing damage, normal stiffness dependence on normal stress, and decrease in the dilation angle with plastic shear displacement (Itasca Consulting Group and Inc 2007). Equation (7) gives the joint shear strength equation. The behavior of the discontinuity interfaces and the fictitious joints is described by the Coulomb-slip joint model (Eq. 8) with the joint stiffnesses given by the two constant parameters  $K_n$  and  $K_s$ .

$$\tau = \sigma_n \tan(\phi + i) \quad (7)$$

$$\tau = \sigma_n \tan \phi \quad (8)$$

**Table 6** Summary of the performed stress analyses cases

Case number	Rock mass system (based on different RMR values)	$K_0$ value	Support system included or not (I/N)
1 (9)	Soft <sup>a</sup>	1.0	N(I)
2 (10)	Average <sup>b</sup>	1.0	N(I)
3 (11)	Stiff <sup>c</sup>	1.0	N(I)
4 (12)	Average	0.5	N(I)
5 (13)	Average	0.75	N(I)
6 (14)	Average	1.25	N(I)
7 (15)	Average	1.5	N(I)
8 (16)	Average	2.0	N(I)

<sup>a</sup>RMR (Oc5) = 36.5, RMR (dike) = 29

<sup>b</sup>RMR (Oc5) = 40, RMR (dike) = 32.5

<sup>c</sup>RMR (Oc5) = 43.5, RMR (dike) = 36

where  $\tau$  is the joint shear stress;  $\sigma_n$  is the joint normal stress;  $\phi$  is the basic friction angle of the joint;  $i$  is the dilation angle.

## 4.2 Stress Analyses Performed in the Numerical Modeling

Because in situ stress measurements were not available for this mine, different  $K_0$  values were assigned to study the effect of the horizontal in situ stress on the rock mass behavior. To study the effect of the variability of rock mass properties on rock mass behavior, three systems (Soft, Average, Stiff) with different RMR values were used to represent different rock mass properties. The specific RMR values used for the three systems are given in Table 6. According to the procedures introduced in Sect. 3, the deformation modulus and strength parameter values of the rock masses in the chosen three RMR systems were different. However, the fault properties were kept constant as given in Table 5. The performance of the bolt supports installed at the mine was evaluated by performing stress analyses under unsupported and supported conditions. All the mentioned cases are summarized in Table 6. Note that Cases 9–16 are the supported conditions for the Cases 1–8, which were run under unsupported conditions.

## 4.3 Results and Discussions

Two vertical planes  $X = 0$  and  $Y = -20$ , as shown in Fig. 3a, were selected to show the representative numerical modeling results. The distances between the tunnels on the planes and the model boundaries are more than eight times of the tunnel dimensions, that means long enough to avoid the boundary effects. Figures 9 and 10 show the stress distributions on the two vertical planes. The negative stress values represent compression. To show the results clearly, only a part around the tunnels are presented. On the plane of  $X = 0$  (Fig. 9), two tunnels exist, labeled as Tunnel 1 and Tunnel 2; the major non-persistent fault goes in between the tunnels; the weak

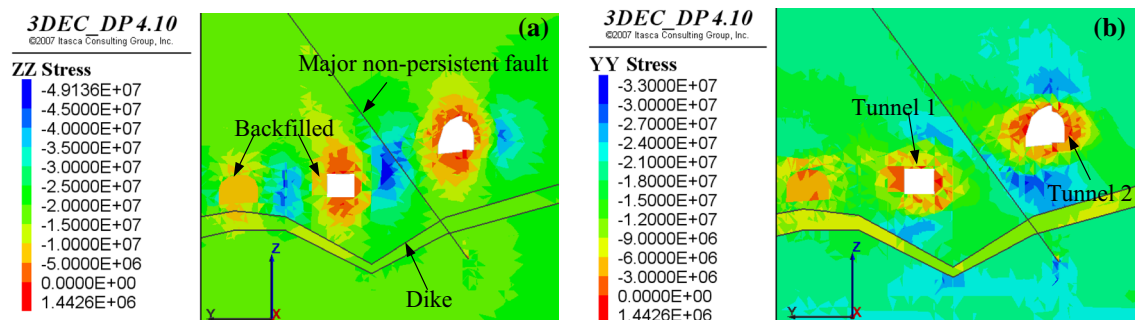


**Fig. 9** Stress distributions for Case 2 on the vertical plane of  $X = 0$  (unit: Pa): **a** vertical stress (ZZ stress) distribution; **b** horizontal stress (YY stress) distribution

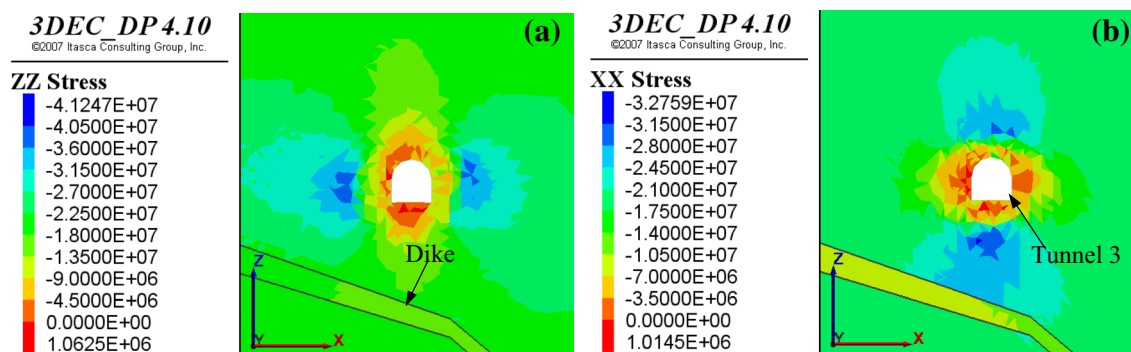


**Fig. 10** Stress distributions for Case 2 on the vertical plane of  $Y = -20$  (unit: Pa): **a** vertical stress (ZZ stress) distribution; **b** horizontal stress (XX stress) distribution

dike layer is located below the two tunnels; the backfilling activities occurred at the left of Tunnel 1. Figure 9a shows that high vertical stresses (ZZ stress) are concentrated on the walls and peaks near the fault; stress relaxation can be observed on the roof and the floor. The horizontal stresses (YY stress) (Fig. 9b), however, are zero on the ribs but high on the roof and the floor; the highest stresses tend to distribute near the dike and the fault. Low horizontal stresses can be seen in the dike layer. On the plane of  $Y = -20$  (Fig. 10), there is only one tunnel (Tunnel 3) with the dike underneath. Under this condition, the stress distributions are less asymmetric compared to that of Fig. 9. The maximum stress values are lower than that around Tunnels 1 and 2. In summary, the distribution of stress around the tunnels agrees with the intuitions, indicating the numerical model behaves correctly under the inputs. Additionally, the influence of the fault and the weak layer on the stress distributions, i.e., asymmetry of stress distributions, is observed.

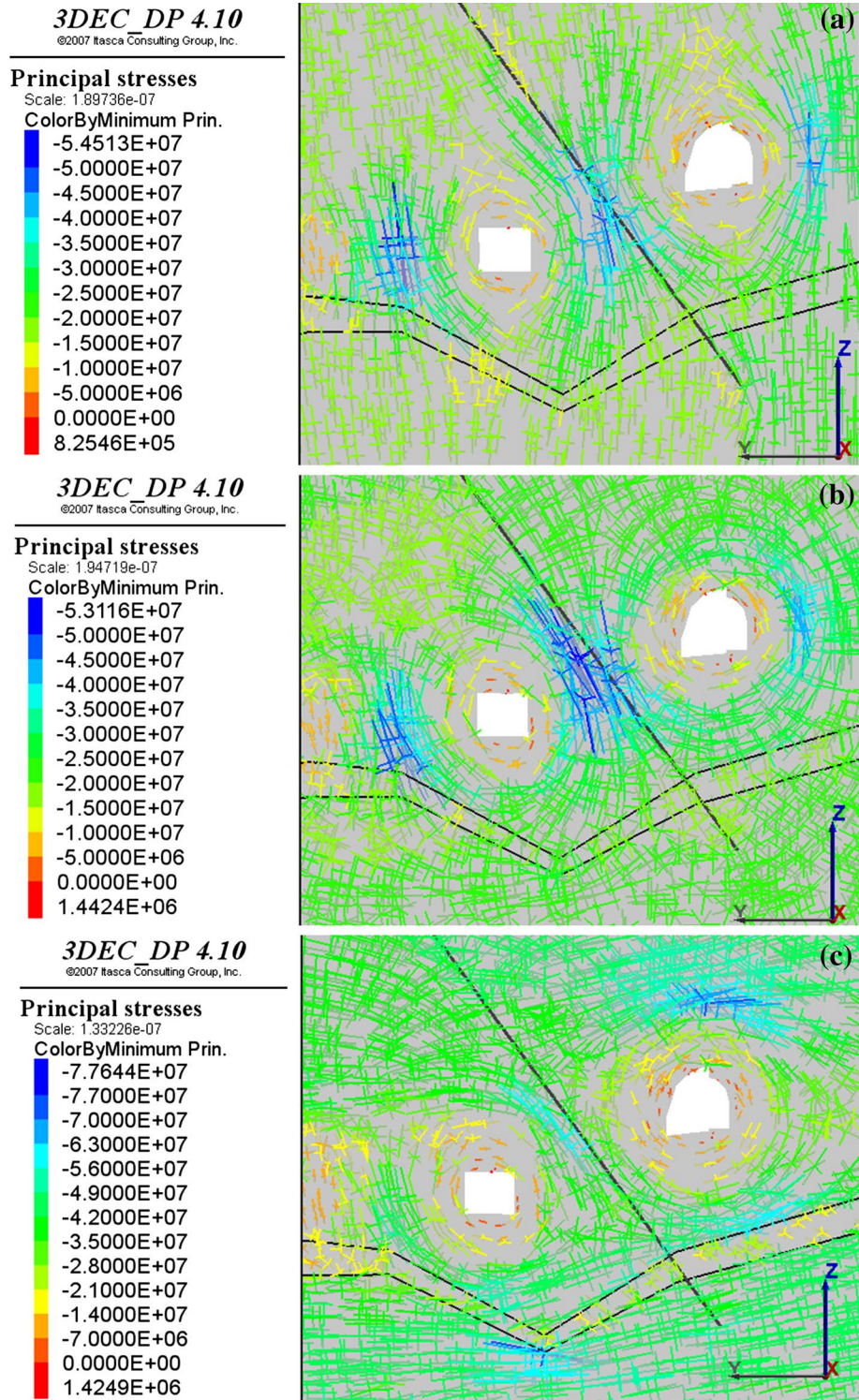
The effect of the lateral in situ stress on rock mass behavior is investigated using the results of Cases 2, and 4–8. Figure 11a–c shows the principal stress distributions for these cases with the  $K_0$  values of 0.5, 1.0, and 2.0 on the plane of  $X = 0$  m. For the low horizontal stress conditions ( $K_0 = 0.5$ ), the stress concentrations occurred near the walls of the two tunnels. Maximum stress values are located at the left rib of Tunnel 1. The stresses on the roof and floor are small with a few positive values (tension). For case 2 (Fig. 11b), the maximum stress has moved to locations near the fault. As  $K_0$  increases to 2.0 (Fig. 11c), the high compressive stresses are appearing on the roofs and the floors, and at locations near the fault and the dike. Stress relaxation can be observed in the dike layer. The weak material is less likely to sustain high stresses, which then is transferred to the adjacent stronger rock masses. The maximum major principal stress reduced at first, to the minimum of 53.1 MPa in Case 2 ( $K_0 = 1.0$ ), and then increased to the maximum of 77.6 MPa in Case 8 ( $K_0 = 2.0$ ). On the plane of  $Y = -20$  (Fig. 12a–c), the distribution of principal stresses is close to symmetric for

low  $K_0$  values (Fig. 12a, b) but less symmetric for high  $K_0$  values (Fig. 12c) due to the existence of the weak layer. The maximum principal stress also minimizes at  $K_0 = 1.0$  and peaks at  $K_0 = 2.0$ . With increasing  $K_0$  values, the maximum major principal stress rotates from the ribs to the roofs and floors of the tunnels; the fault plays a role on the stress in low  $K_0$  cases, while the influence of the fault and the dike is more pronounced for high  $K_0$  cases.

Plots in Figs. 13 and 14 show the variations of the horizontal and vertical convergences of the tunnels, respectively. Different colors of the lines represent the results around the three tunnels. The displacements used to calculate the convergence were taken from the middle of the roof, ribs, and floor of the tunnels. Results show that most of the convergences, in both directions, increase slightly from  $K_0 = 0.5$  to 1.25 but significantly from  $K_0 = 1.25$  to 2.0. For Tunnel 1, due to the fact that the left rib was backfilled, the value of the horizontal convergence in Fig. 13 (in blue color) is less than that of other two tunnels. For Tunnels 2 and 3, the results show that at low  $K_0$  values, 0.5 and 0.75, for example, the horizontal convergences are slightly higher than the vertical convergences; at high  $K_0$  values (2.0), the tunnels, however, are suffering from more vertical convergences.

Instead of using the conventional failure index that is given for the strain-softening model in 3DEC, the rock masses that reach their residual strength, either in compression or tension, are considered as failed in this paper. The results showed that most of the failure around the tunnels is shear failure. To effectively describe the failed area, measurements were taken at three locations on each surface and then averaged as the thicknesses, as shown in Figs. 15 and 16. The change of failure zone thicknesses on the ribs (Fig. 15) is not monotonic, but most of them slightly reduced from  $K_0 = 0.5$  to  $K_0 = 2.0$ . However, Fig. 16 shows that the failure zone thicknesses on the roofs and floors of the tunnels keep increasing when the  $K_0$  value increases. These changes coincide with the results of the stress variations presented in Figs. 11 and 12 that the cases with high  $K_0$  values have

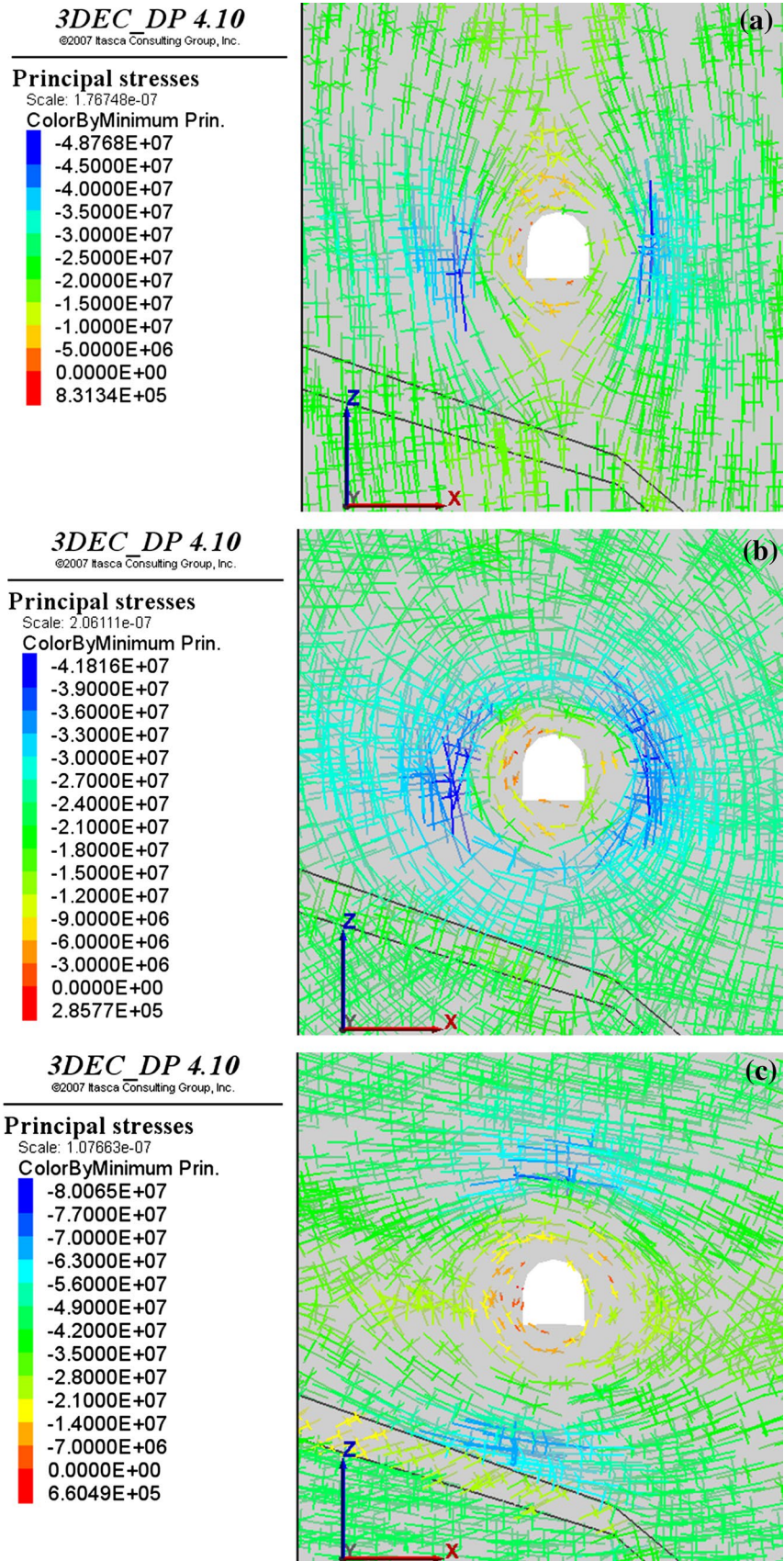
**Fig. 11** Principal stress distributions for cases with different  $K_0$  values on the vertical plane of  $x = 0$  m (unit: Pa): **a** Case 4 ( $K_0 = 0.5$ ); **b** Case 2 ( $K_0 = 1.0$ ); **c** Case 8 ( $K_0 = 2.0$ )



unfavorable roof and floor conditions but relatively stable ribs. Conversely, for low  $K_0$  cases, i.e., 0.5 and 0.75, major safety concerns are taking place on the ribs than on the roofs and floors (Figs. 15 and 16). It can be noticed that the deformations at the left rib of Tunnel 2 and the right rib of Tunnel 1 on plane of  $X = 0$  (red and blue results in Fig. 15) are

higher than that at other places. It may be ascribed for the close distance to the major fault (Fig. 9). For Tunnel 3, the rock masses on the floor are undergoing more failure than that on the roof (yellow and dark blue results in Fig. 16), which is likely due to the influence of the dike located below the floor (Fig. 10).

**Fig. 12** Principal stress distributions for cases with different  $K_0$  values on the vertical plane of  $y = -20$  m (unit: Pa): **a** Case 4 ( $K_0 = 0.5$ ); **b** Case 2 ( $K_0 = 1.0$ ); **c** Case 8 ( $K_0 = 2.0$ )



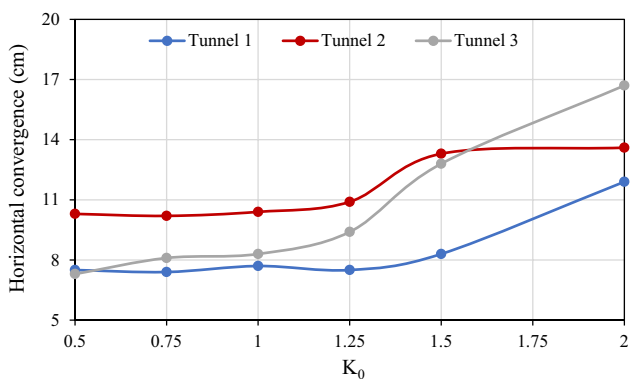


**Fig. 13** Horizontal convergence of the tunnels for cases with different  $K_0$  values

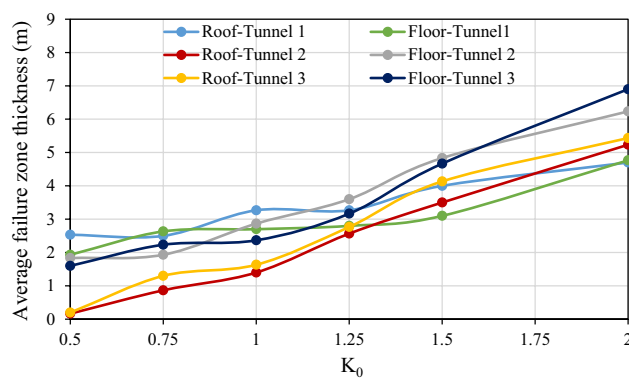


**Fig. 16** Average failure zone thicknesses on the roofs and floors of the tunnels for cases with different  $K_0$  values

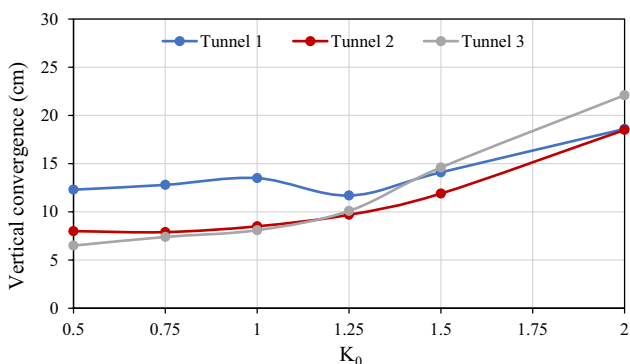


**Fig. 14** Vertical convergence of the tunnels for cases with different  $K_0$  values

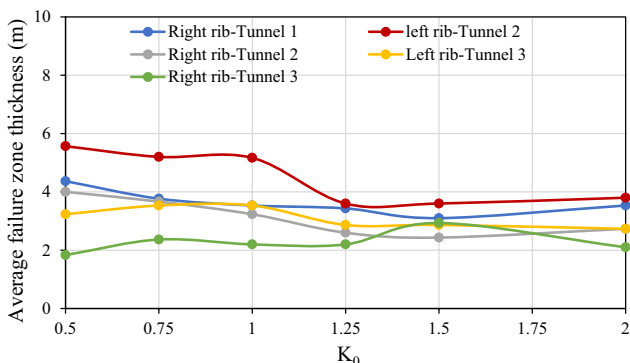


**Fig. 15** Average failure zone thicknesses on the ribs of the tunnels for cases with different  $K_0$  values

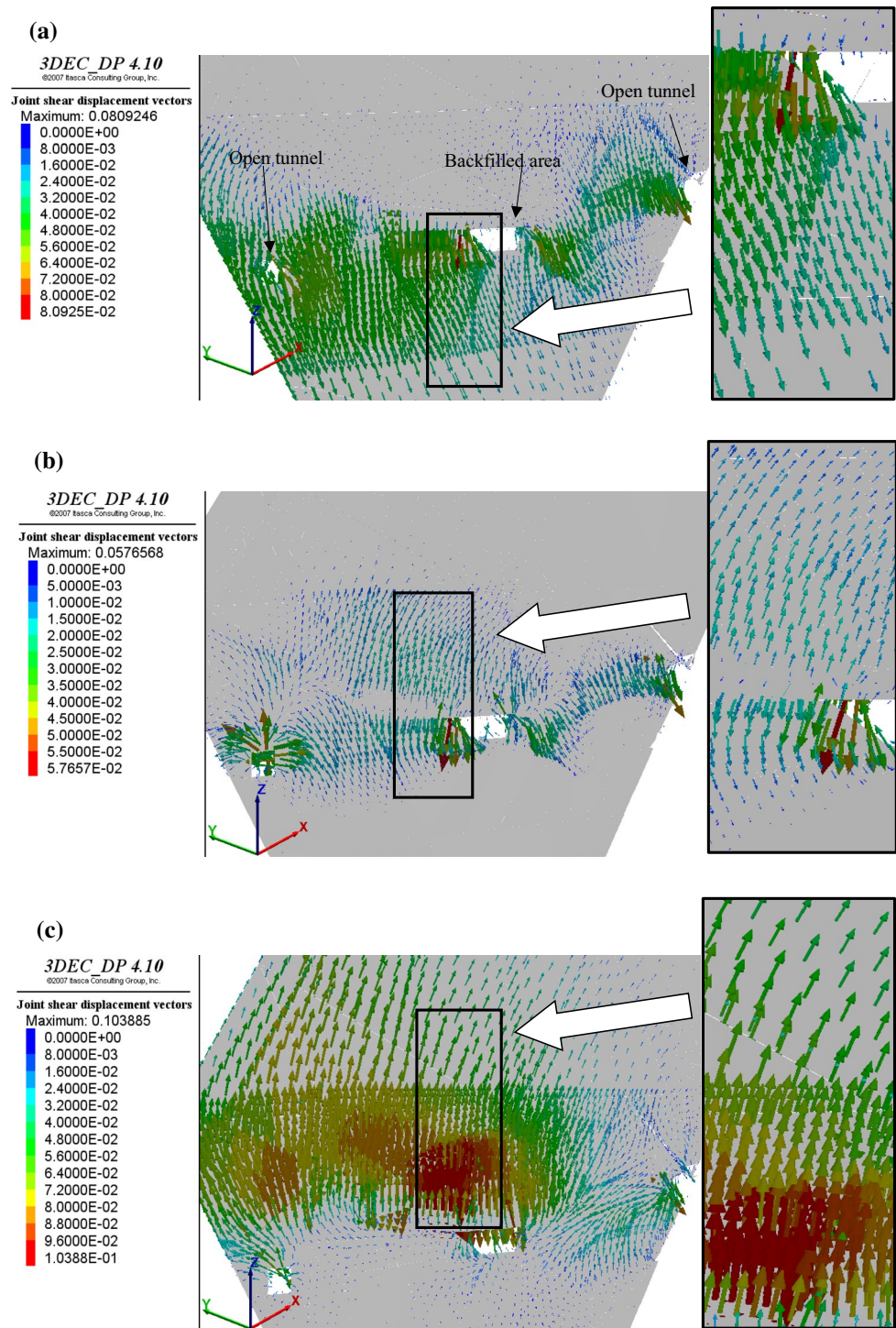
Figure 17a–c shows the joint shear behavior of the major non-persistent fault for Cases 4, 2, and 8. The vectors represent the shear displacements of the hanging wall plane of the fault (Fig. 3a). To show the results clearly, a selected area in each plot is enlarged. For Case 4 ( $K_0 = 0.5$ ), the fault

hanging wall moves downwards; displacements are mainly occurring at the lower half plane; the maximum value of 8.1 cm is located at the backfilled region (Fig. 17a). For Case 2 ( $K_0 = 1.0$ ), the fault shear displacements become smaller; slight movements toward up can be observed at the upper part, while the lower part is moving down; the maximum value of 5.8 cm is still near the backfilled region (Fig. 17b). As  $K_0$  increases to 2.0 (Fig. 17c), the fault plane, however, shows distinct movements to up; the maximum displacement is 10.4 cm, above the backfilled area. Figure 18 shows the maximum shear displacements (see the legends of Fig. 17) for the different cases, where Cases 2 ( $K_0 = 1.0$ ) and 6 ( $K_0 = 1.25$ ) give lowest values. The  $K_0$  value significantly changes the shear displacement of the major non-persistent fault in both direction and magnitude. This change would result in totally different reactions on the rock mass in the numerical model, contributing to the deformations and failures of the surrounding excavations.

To take into account the possible variation of RMR values, the soft, average, and stiff rock mass systems were considered. Results can be found in Figs. 19 and 20. The multiple locations around the tunnels are marked on the horizontal axis of Figs. 19 and 20. It is obvious that Case 1 (soft) with the lowest rock mass properties results in the largest deformations (Fig. 19), approximately three times that of Case 3 (Stiff). Due to the presence of backfilling activities and major fault on the vertical plane of  $X = 0$ , the deformations around the Tunnels 1 and 2 are larger than that around the Tunnel 3. The behavior is more distinct in the soft case (blue results in Fig. 19). Figure 20 shows that the soft system has the largest failed area around the tunnels as almost twice that of the stiff system. Large failure area can be observed at the two locations close to the major fault (right wall of Tunnel 1 and left wall of Tunnel 2).

The effect of the support system is evaluated by comparing the results between Cases 1–3 and that of Cases 9–11 (see Table 6). Figure 21 shows the reduction in the

**Fig. 17** Joint shear displacement vectors along the fault for cases with different  $K_0$  values (unit: m) (observed from the hanging wall direction): **a** Case 4 ( $K_0 = 0.5$ ); **b** Case 2 ( $K_0 = 1$ ); **c** Case 8 ( $K_0 = 2.0$ )



maximum displacements around the tunnels comparing between supported and unsupported cases. Most of the displacements have reduced 2–8% after applying the supports, and several zero reductions appear at the floors. This situation is reasonable since no support was installed on the floor of the tunnels. For two locations, maximum displacement reductions in the range of 15–20% appear. Figure 22 gives

the reduction in the thicknesses of the failure zone around the tunnels. The reductions are clustered around the level 10%, higher than that of the displacements. However, more zero improvements can be observed.

The safety of rock supports is addressed by the bond shear failure and bolt tension failure conditions. In 3DEC, the failure condition of bond/grout is evaluated using the bond

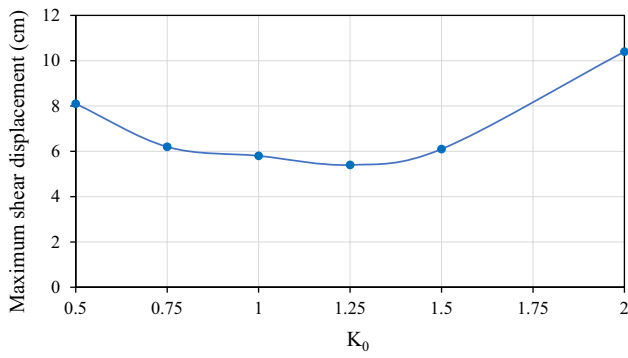


**Fig. 18** Maximum shear displacement on the fault plane for cases with different  $K_0$  values

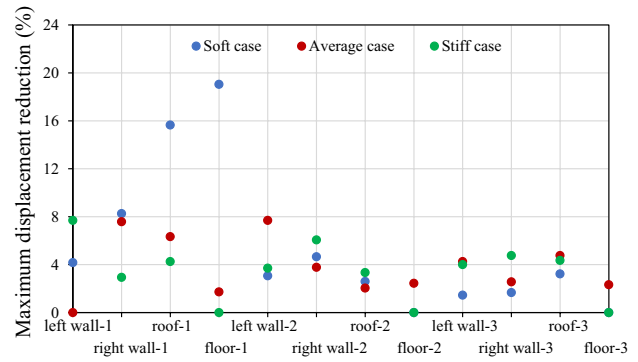


**Fig. 21** Reduction in maximum displacement around the tunnels after the installation of the support system

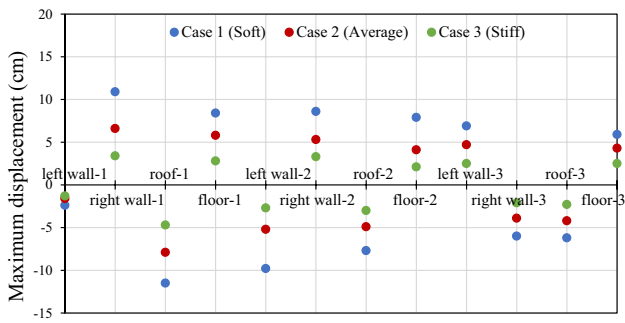


**Fig. 19** Maximum displacements around the tunnels for different rock mass systems

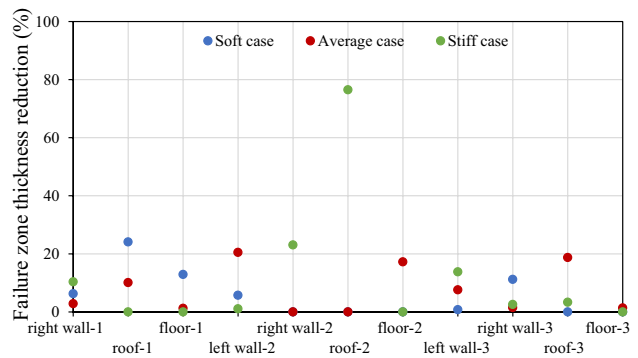


**Fig. 22** Reduction in the failure zone thickness around the tunnels after the installation of the support system

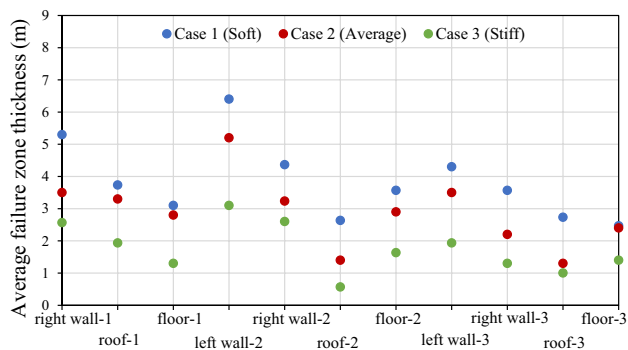


**Fig. 20** Average thicknesses of the failure zone around the tunnels for different rock mass systems

shear strength rather than the bond slip. Once the shear force developed in the bond/grout, which is related to the bond/grout shear stiffness and the relative displacement between the reinforcement and the rock mass, exceeds the bond/grout shear capacity (strength multiplied by the shear area), the bond is marked as failure. Figure 23 shows the state of bond failure for a part of representative bolt supports for Case 10. Bond shear failure is mostly taking place on the short bolts on the ribs (split sets) and the short ones on the roof (resin

bolts). On the contrary, the bond of longer bolts either on the ribs (swellex bolts) or on the roof (swellex and cable bolts) is safe and shown as intact (in blue color). Figure 24 shows the axial force distribution of the supports. Unlike the bond failure, the longer bolts and the short roof bolts (resin bolts) have higher axial forces (red color), while the forces of short wall bolts (split sets) are small. To present the failure condition for the whole support system, the percentages of the bond shear failure and of the bolt tension failure are given for all supported cases and are shown in Table 7. The values were calculated based on the bolt information exported from the software. To be on the conservative side, the bolts having the axial force close to the tensile yield capacity within 1 kN are considered as failure. Results show that 88–92% of the split sets and 60–80% of the resin bolts have failed in shear, corresponding to that presented in Fig. 23. On the other hand, 10–45% of the resin bolt and 45–60% of the swellex bolts have failed in tension. The bond condition is related to the bolt length, the grout, or the contact between the bolts and the rock masses. It can be observed from Figs. 15 and 20 that the failure zone thicknesses on ribs are mainly in the range of 2–5 m, which is much larger than

**Fig. 23** State of bond failure of the applied bolt supports for Case 10

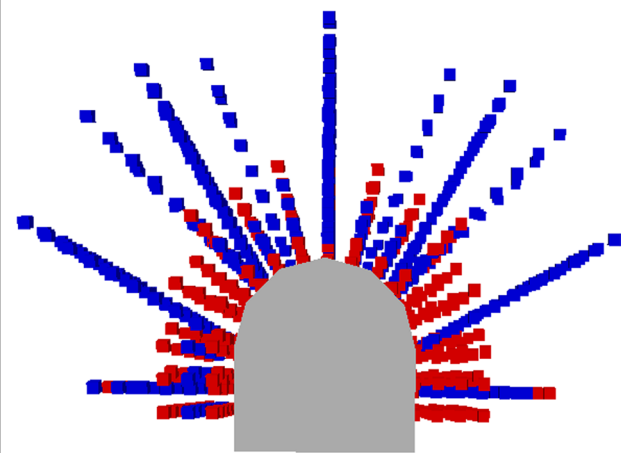
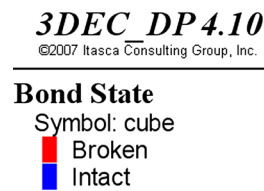


**Fig. 24** Axial force of the applied supports for Case 10 (unit: N)

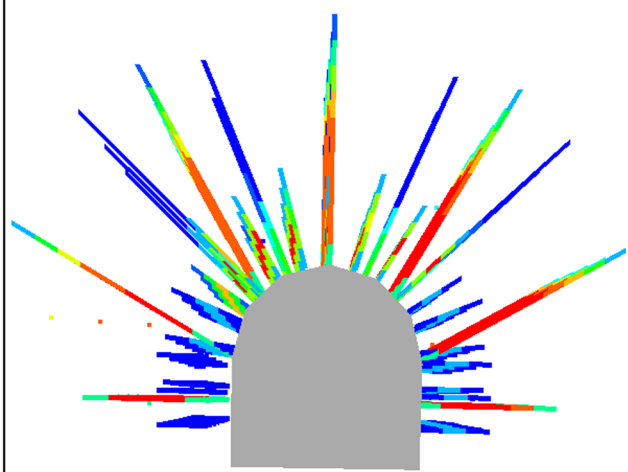
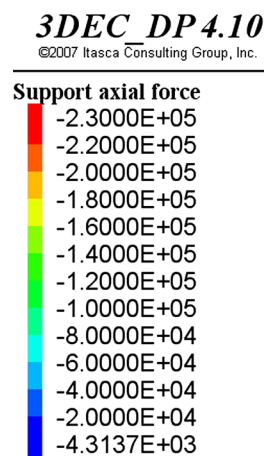


**Table 7** Failure conditions for the different supports

Case no.	Bond shear failure (%)				Bolt tensile failure (%)			
	Split sets	Resin bolts	Cable bolts	Swellex bolts	Split sets	Resin bolts	Cable bolts	Swellex bolts
9	88	73	0	18	0	35	20	52
10	89	73	0	15	0	33	0	52
11	88	62	0	10	0	18	2	61
12	92	61	0	15	0	11	3	45
13	91	65	0	15	0	16	3	55
14	88	76	0	16	0	41	11	53
15	88	76	0	18	0	43	21	57
16	88	80	0	21	0	34	39	63

the length of split sets (1.83 m). Similarly, some roofs have the failure zone thickness (Figs. 16, 20) larger than 2.4 m, which is the length of resin bolts. The two types of bolts are hence insufficient in length. Table 7 also shows the tension condition of the bolts; the roof resin and swellex bolts are in bad condition. More failures can be observed in the soft

rock mass and high  $K_0$  cases, where the roof problems are distinct (Figs. 16, 20). For those situations, the stronger and denser bolts may be needed.

Because the instantaneous installation was simulated, the effectiveness of rock supports was compromised from the real situation. It is possible that the delayed supporting



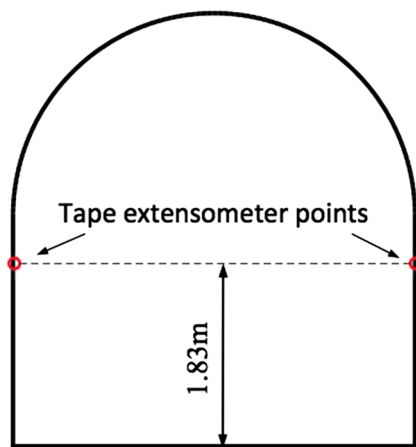


**Fig. 25** Sketch of the tunnel cross section with field instruments

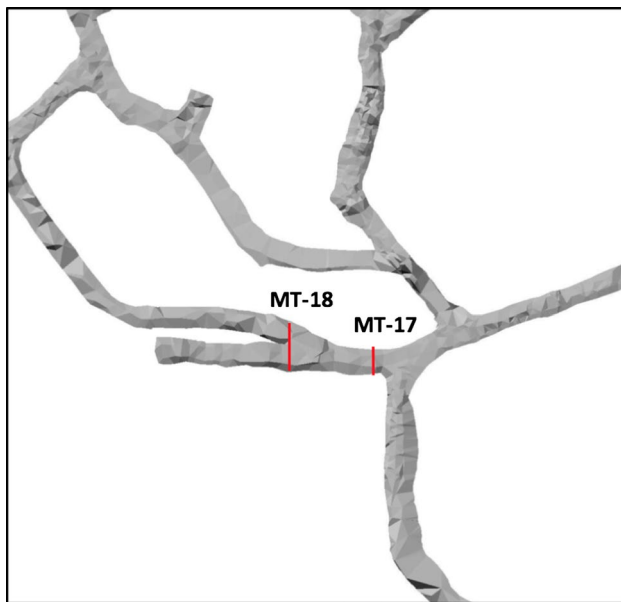


**Fig. 26** Plan view of the locations of the field instruments in relation to the tunnel system

would result in another 5–10% reduction for both deformations and failure areas around the tunnels as well as a slight improvement in the safety of the supports.

Tape extensometers were applied at this mine at many locations to monitor the horizontal tunnel convergence. Figure 25 shows the tunnel cross section sketch with the extensometers. MT-17 and MT-18, as shown in Fig. 26, are the two interested locations where the monitored convergences were larger than that at other locations. Due to the geometry difference between the tunnels built in the numerical model and that in the field, the convergence strain (tunnel convergence over tunnel geometry) is utilized. Comparisons are made between the numerical modeling results and the

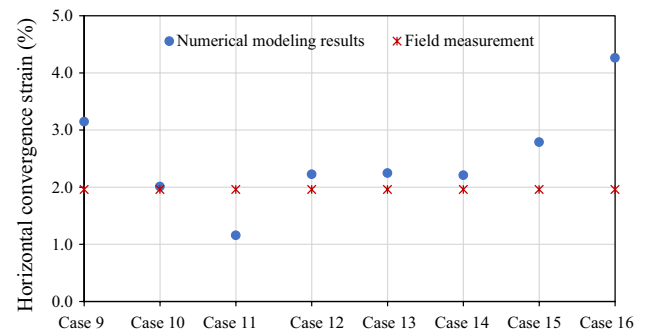


**Fig. 27** Comparisons between the numerical modeling results and field measurement at MT-17

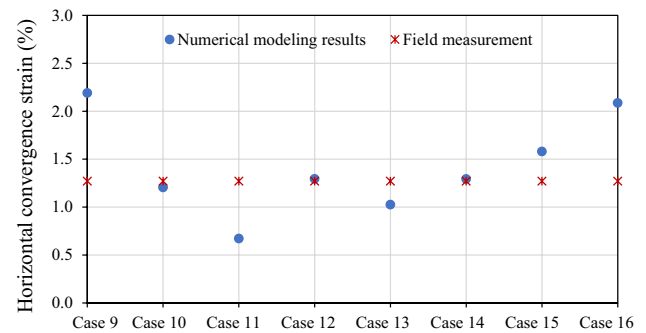


**Fig. 28** Comparisons between the numerical modeling results and field measurement at MT-18

field measurements, as shown in Figs. 27 and 28. The asterisks represent the field measurements, and the dots are the predicted results for various cases. It can be observed that the soft system (Case 9) gives higher results, while the stiff system (Case 11) gives lower results than the field measurements. In addition, the cases with high horizontal in situ stresses [Cases 15 ( $K_0 = 1.5$ ) and 16 ( $K_0 = 2.0$ )] seem not applicable for this mine. The results of Cases 10, 12–14 (average systems with  $K_0$  values between 0.5 and 1.25) are quite close to the field measurements.

## 5 Conclusions

In this paper, the tunnel stability in an underground mine was investigated by three-dimensional discontinuum numerical modeling. The numerical model was developed using the available geological and mine construction information, which contains the complex lithologies, the large-scale discontinuities, and a complex tunnel system. The rock mass properties that represent the combined properties of the intact rock and minor discontinuities were estimated using the empirical formulas, based on

the laboratory test results of the intact rock and the field rock mass characteristics. The strain-softening block and continuously yielding joint models were prescribed for the rock masses and the faults, respectively, in the numerical model.

The effect of the horizontal in situ stress on the rock mass stability was studied by performing stress analyses on the cases with different  $K_0$  values. As  $K_0$  increases, the maximum major principal stress direction rotates from the ribs to the roofs and floors; the value decreased at first but then increased. Both the vertical and horizontal convergence of the tunnels increased with the increasing  $K_0$  values. Most of the failure zone thicknesses on the ribs reduced a little bit but increased a lot on the roofs and the floors. The shear displacements of the major fault were greatly changed in both the direction and the magnitude with the varying  $K_0$  value. All the results indicate that the cases with  $K_0 = 1.0$  are most stable, having the lowest stresses and small fault deformations; tunnels in the case with  $K_0$  of 1.5 and 2.0, however, are unstable with severe roof and floor problems. The rock mass behavior was affected by the major fault and the weak dike layer, and the influence is more pronounced in high  $K_0$  cases.

The soft, average, and stiff systems were simulated to account for the possible variation of the RMR values of the lithologies. Results showed that the tunnels in the soft system with the weakest material property values are the most unstable, while the stiff system led to the smallest deformations and failure zones around the tunnels.

The rock supports were evaluated using the quantified rock mass behavior and the quantified failure conditions of the supports. Application of the rock supports slightly controlled the deformations and the failure zones around the tunnels. Most of the short bolts failed in bond shear while longer bolts indicated tendency to failure in tension with respect to bolt itself. Strengthening the support system with longer bolts on the ribs is a priority; denser arrangements and stronger supports might be also needed to improve the safety of the rock mass and the supports.

Finally, the numerical modeling results were compared with the field measurements at two locations. The results of the average rock mass property systems with the  $K_0$  values from 0.5 to 1.25 agree well with the field measurements.

**Acknowledgements** The research was funded by the Centers for Disease Control and Prevention under the Contract No. 200-2011-39886. The support provided by the mining company through providing geological and geotechnical data, rock core and mine technical tours, and allowing access to the mine to perform field investigations is very much appreciated. The first author is grateful to the Chinese Scholarship Council and the University of Arizona Graduate College for providing scholarships to conduct the research described in this paper as a Ph.D. student at the University of Arizona.

## References

- Alejano LR, Alfonso RD, Veiga M (2012) Plastic radii and longitudinal deformation profiles of tunnels excavated in strain-softening rock masses. *Tunn Undergr Space Technol* 30:169–182
- Bandis S, Lumsden AC, Barton NR (1983) Fundamentals of rock joint deformation. *Int J Rock Mech Min Sci Geomech Abstr* 20(6):249–268
- Barla G, Barla M (2000) Continuum and discontinuum modeling in tunnel engineering. *Min Geol Pet Eng Bull* 12:45–57
- Barton N, Choubey V (1977) The shear strength of rock joints in theory and practice. *Rock Mech* 10:1–54
- Bhasin R, Høeg K (1997) Parametric study for a large cavern in jointed rock using a distinct element model (UDEC-BB). *Int J Rock Mech Min Sci* 35(1):17–29
- Bhasin R, Magnussen AW, Grimstad E (2006) The effect of tunnel size on stability problems in rock masses. *Tunn Undergr Space Technol* 21:405
- Bieniawski ZT (1976) Rock mass classifications in rock engineering. In: *Proceedings symposium on exploration for rock engineering, Johannesburg* 1:97–106
- Cai M (2008) Influence of stress path on tunnel excavation response—Numerical tool selection and modeling strategy. *Tunn Undergr Space Technol* 23:618–628
- Cantieni L, Anagnostou G (2009) The effect of the stress path on squeezing behavior in tunneling. *Rock Mech Rock Eng* 42:289–318
- Chryssanthakis P, Barton N, Lorig L, Christianson M (1997) Numerical simulation of fiber reinforced shotcrete in tunnel using the discrete element method. *Int J Rock Mech Min Sci* 34:54.e1–54.e14
- Cui Z, Sheng Q, Leng X (2016) Control effect of a large geological discontinuity on the seismic response and stability of underground rock caverns: a case study of Baihetan #1 surge chamber. *Rock Mech Rock Eng* 49:2099–2114
- Cundall PA (1971) A computer model for simulating progressive, large-scale movements in blocky rock systems. In: *Proceedings of the international symposium rock fracture. ISRM Proceedings* 2:129–136
- Cundall PA (1980) UDEC-A generalized distinct element program for modelling jointed rock. Report from P. Cundall Associates to U.S. Army European Research Office, London
- Cundall PA (1988) Formulation of a three-dimensional distinct element model—part I. A scheme to detect and represent contacts in a system composed of many polyhedral blocks. *Int J Rock Mech Sci Geomech* 25:107–116
- Egger P (2000) Design and construction aspects of deep tunnels (with particular emphasis on strain softening rocks). *Tunn Undergr Space Technol* 15(4):403–408
- Fekete S, Diederichs M (2013) Integration of three-dimensional laser scanning with discontinuum modelling for stability analysis of tunnels in blocky rock masses. *Int J Rock Mech Min Sci* 57:11–23
- Gao F, Stead D, Kang H (2014) Simulation of roof shear failure in coal mine roadways using an innovative UDEC Trigon approach. *Comput Geotech* 61:33–41
- Gens A, Carol I, Alonso EE (1989) An interface element formulation for the analysis of soil-reinforcement interaction. *Comput Geotech* 7:133–151
- Ghaboussi J, Wilson EL, Isenberg J (1973) Finite element for rock joints and interfaces. *J Soil Mech Div ASCE* 99(SM10):833–848
- Goodman, RE (1974) The mechanical properties of joints. In: *Proceedings of the third international congress of the international society of rock mechanics, Denver, Colorado* 1:127–140
- Goodman RE, Taylor RL, Brekke TL (1968) A model for the mechanics of jointed rock. *J Soil Mech Found Div ASCE* 94(SM3):637–659

- Hajiabdolmajid V, Kaiser PK, Martin CD (2002) Modelling brittle failure of rock. *Int J Rock Mech Min Sci* 39:731–741
- Hao YH, Azzam R (2005) The plastic zones and displacements around underground openings in rock masses containing a fault. *Tunn Undergr Space Technol* 20:49–61
- Hart R, Cundall PA, Lemos J (1988) Formulation of a three-dimensional distinct element model—part II. Mechanical calculations for motion and interaction of a system composed of many polyhedral blocks. *Int J Rock Mech Min Sci Geomech Abstr* 25(3):117–125
- Hoek E (1994) Strength of rock and rock masses. *ISRM News J* 2:4–16
- Hoek E, Brown ET (1997) Practical estimates of rock mass strength. *Int J Rock Mech Min Sci* 34:1165–1186
- Hoek E, Diederichs MS (2006) Empirical estimation of rock mass modulus. *Int J Rock Mech Min Sci* 43:203–215
- Hoek E, Carranza-Torres C, Corkum B (2002) Hoek–Brown criterion—2002 edition. In: *Proceedings of NARMS-TAC conference, Toronto*, 1:267–273
- Huang F, Zhu H, Xu Q, Cai Y, Zhuang X (2013) The effect of weak interlayer on the failure pattern of rock mass around tunnel—Scaled model tests and numerical analysis. *Tunn Undergr Space Technol* 35:207–218
- Huang G, Kulatilake PHSW, Shreedharan S, Cai S, Song H (2017) 3-D discontinuum numerical modeling of subsidence incorporating ore extraction and backfilling operations in an underground iron mine in China. *Int J Min Sci Tech* 27:191–201
- Itasca Consulting Group, Inc (2007) 3DEC-3 dimensional distinct element code, version 4.1
- Jia P, Tang CA (2008) Numerical study on failure mechanism of tunnel in jointed rock mass. *Tunn Undergr Space Technol* 23:500–507
- Jing L (2003) A review of techniques, advances and outstanding issues in numerical modeling for rock mechanics and rock engineering. *Int J Rock Mech Min Sci* 40:283–353
- Kulatilake PHSW, Ucpirti H, Wang S, Radberg G, Stephansson O (1992) Use of the distinct element method to perform stress analysis in rock with non-persistent joints and to study the effect of joint geometry parameters on the strength and deformability of rock masses. *Rock Mech Rock Eng* 25:253–274
- Kulatilake PHSW, Park JY, Um JG (2004) Estimation of rock mass strength and deformability in 3-D for a 30 m cube at a depth of 485 m at Äspö hard rock laboratory. *Geotech Geol Eng* 22:313–330
- Kulatilake PHSW, Wu Q, Yu ZX, Jiang FX (2013) Investigation of stability of a tunnel in deep coal mine in China. *Int J Min Sci Technol* 23:579–589
- Kulatilake PHSW, Shreedharan S, Sherizadeh T, Shu B, Xing Y, He P (2016) Laboratory estimation of rock joint stiffness and frictional parameters. *Geotech Geol Eng* 34(6):1723–1735
- Li JC, Li HB, Ma GW, Zhou YX (2013) Assessment of underground tunnel stability to adjacent tunnel explosion. *Tunn Undergr Space Technol* 35:227–234
- Lin P, Liu H, Zhou W (2015) Experimental study on failure behavior of deep tunnels under high in situ stresses. *Tunn Undergr Space Technol* 46:28–45
- Malama B, Kulatilake PHSW (2003) Models for normal fracture deformation under compressive loading. *Int J Rock Mech Min Sci* 40:893–901
- Ray AK (2009) Influence of cutting sequence and time effects on cutters and roof falls in underground coal mine—numerical approach. Dissertation, West Virginia University
- Shen B, Barton N (1997) The disturbed zone around tunnels in jointed rock masses. *Int J Rock Mech Min Sci* 34(1):117–125
- Shreedharan S, Kulatilake PHSW (2016) Discontinuum-equivalent continuum analysis of the stability of the stability of tunnels in a deep coal mine using the distinct element method. *Rock Mech Rock Eng* 49:1903–1922
- Souley M, Homand F, Thoraval A (1997) The effect of joint constitutive laws on the modelling of an underground excavation and comparison with in situ measurements. *Int J Rock Mech Min Sci* 34(1):97–115
- Tan WH, Kulatilake PHSW, Sun HB (2014a) Influence of an inclined rock stratum on in situ stress state in an open-pit mine. *Geotech Geol Eng* 32:31–42
- Tan WH, Kulatilake PHSW, Sun HB (2014b) Effect of faults on in situ stress state in an open-pit mine. *Electron J Geotech Eng* 19:9597–9629
- Wang X, Kulatilake PHSW, Song WD (2012) Stability investigations around a mine tunnel through three-dimensional discontinuum and continuum stress analyses. *Tunn Undergr Space Technol* 32:98–112
- Wu Q, Kulatilake PHSW (2012) REV and its properties on fracture system and mechanical properties, and an orthotropic constitutive model for a jointed rock mass in a dam site in China. *Int J Comput Geotech* 43:124–142
- Xing Y, Kulatilake PHSW, Sandbak LA (2017) Rock mass stability investigation around tunnels in an underground mine in USA. *Geotech Geol Eng* 35:45–67
- Zhu W, Zhao J (2004) Stability analysis and modelling of underground excavations in fractured rocks. In: Hudson JA (ed) *Elsevier geo-engineering book series, geo-engineering book series, vol 1*. Elsevier, Oxford, pp 1–5
- Zienkiewicz OC, Best B, Dullage C, Stagg K (1970) Analysis of non-linear problems in rock mechanics with particular reference to jointed rock systems. In: *Proceedings of the second international congress on rock mechanics, Belgrade*, 3: 501–509